NORDITA-2015-69

Rheology of confined non-Brownian suspensions

Walter Fornari,[1] Luca Brandt,[1] Pinaki Chaudhuri,[2] Cyan Umbert Lopez,[1] Dhrubaditya Mitra,[3] and Francesco Picano[4]

[1] *Linné Flow Centre and SeRC, KTH Mechanics, SE-100 44 Stockholm, Sweden*
[2] *Institute of Mathematical Sciences, CIT Campus, Taramani, Chennai 600113, India*
[3] *Nordita, KTH Royal Institute of Technology and Stockholm University, Roslagstullsbacken 23, 10691 Stockholm, Sweden*
[4] *Department of Industrial Engineering, University of Padova, Via Venezia 1, 35131, Padova, Italy*

(Dated: June 30, 2015,)

We study the rheology of confined suspensions of neutrally buoyant rigid monodisperse spheres in plane-Couette flow using Direct Numerical Simulations. We find that if the width of the channel is a (small) integer multiple of the sphere's diameter, the spheres self-organize into two-dimensional layers that slide on each other and the suspension's effective viscosity is significantly reduced. Each two-dimensional layer is found to be structurally liquid-like but their dynamics is frozen in time.

arXiv:1506.08722v1 [cond-mat.soft] 29 Jun 2015

Suspensions of solid objects in simple Newtonian solvents (e.g., water) can show a kaleidoscope of rheological behaviors depending on the shape, size, volume fraction (ϕ) of the additives, and the shear-rate ($\dot{\gamma}$) imposed on the flow; see, e.g., Refs. [1, 2] for reviews. Suspensions can be of various types, e.g., suspensions of small particles (smaller than the viscous scale of the solvent), where the solvent plays the role of a thermal bath, are called Brownian suspensions (e.g. colloids) [1]. At small ϕ and under small $\dot{\gamma}$, the effective viscosity of such suspensions increases with ϕ: $\mu_{\rm eff} \sim (5/2)\phi$ [3], as derived by Einstein [4] (See also Ref. [5] for a d dimensional generalization). In the other category are suspensions of large particles (e.g. emulsion, granular fluids etc.), where the thermal fluctuations are often negligible. Such suspensions are called *non-Brownian* suspensions. For moderate values of ϕ and $\dot{\gamma}$ non-Brownian suspensions show *continuous shear-thickening*, (i.e., $\mu_{\rm eff}$ increases with $\dot{\gamma}$) [6, 7] which can be understood [7] in terms of excluded volume effects. Such a rheological response has been observed in many natural and industrial flows, including flows of mud, lava, cement, and cornstarch solutions. Dense (large ϕ, close to random close packing) non-Brownian suspensions may show *discontinuous shear-thickening* [8, 9] – a jump in effective viscosity as a function of $\dot{\gamma}$.

Recent experiments have uncovered intriguing rheological behavior of very dense (large ϕ) suspensions under confinement [6, 8, 10]. Common wisdom dictates that, under confinement, the inertial effects are generally unimportant at small $\dot{\gamma}$. But a series of recent studies [11–14] have demonstrated that the effect of fluid inertia, although small, can give rise to variety of effects even in microfluidic flows. Drawing inspirations from these two sets of works, in this paper, we study the effects of confinement on non-Brownian suspensions with moderate values of ϕ and $\dot{\gamma}$. In particular, we choose the range of ϕ and $\dot{\gamma}$ such that in bulk the suspensions show continuous shear-thickening.

As a concrete example, we consider direct numerical simulations (DNS) of three-dimensional plane-Couette flow – with the x, y and z coordinates along the stream-wise, span-wise and wall-normal directions respectively [see Fig. (1a)] – embedded with neutrally-buoyant rigid spheres of radius a. The fluid phase is described by solving the incompressible Navier–Stokes equations in three dimensions. The fluid is sheared by imposing constant stream-wise velocity of opposite signs, $U_0 = \dot{\gamma} L_z/2$ at $z = \pm L_z/2$. Periodic boundary conditions are imposed on the other two directions (x and y with lengths L_x and L_y respectively). The motion of the rigid spheres and their interaction with the flow is fully resolved by using the Immersed Boundary Method [15, 16]. A description of the equations and the details of the algorithm is provided as supplemental material.

We study the effects of confinement by changing the dimensionless ratio $\xi \equiv L_z/2a$, where L_z is the channel width in the z direction. In practice, we change L_z but hold the particle radius a fixed. The effective viscosity, $\mu_{\rm eff}$, is thus function of the dimensionless numbers, ϕ, ξ and the particle Reynolds number, ${\rm Re} \equiv \rho\dot{\gamma}a^2/\mu_{\rm f}$, where ρ and $\mu_{\rm f}$ are the density and dynamic viscosity of the solvent. The most striking result of our simulations is that at or near integer values of ξ, $\mu_{\rm eff}$ decreases significantly compared to its bulk value; see Fig. (1b). This drop can be so large that the net rate of mass transport for a thinner channel ($\xi = 2$) is more than in a wider channel ($\xi = 2.5$), see Fig. (1c). We further demonstrate that, at small integer values of ξ, the rigid spheres self-organize into an integer number of horizontal layers, which slide on one another, see Fig. (2). This, in turn, decreases the transport of horizontal momentum across the layers generating the drop in effective viscosity. We also show that at integer values of ξ, for which layers appear: (a) the movement of spheres across layers is *not* a diffusive process, Fig. (3), (b) the typical residence time of the spheres in a layer is much longer than the time scale set by the shear, $\dot{\gamma}^{-1}$; in fact, a large number of spheres never leave the layer within the runtime of the simulations Fig. (4a); (c) the layers are structurally liquid-like but dynamically very slow compared to the timescale set by $\dot{\gamma}^{-1}$, see Fig. (4).

Initially, the spheres are placed at random locations, with no overlap between each other, and with velocities

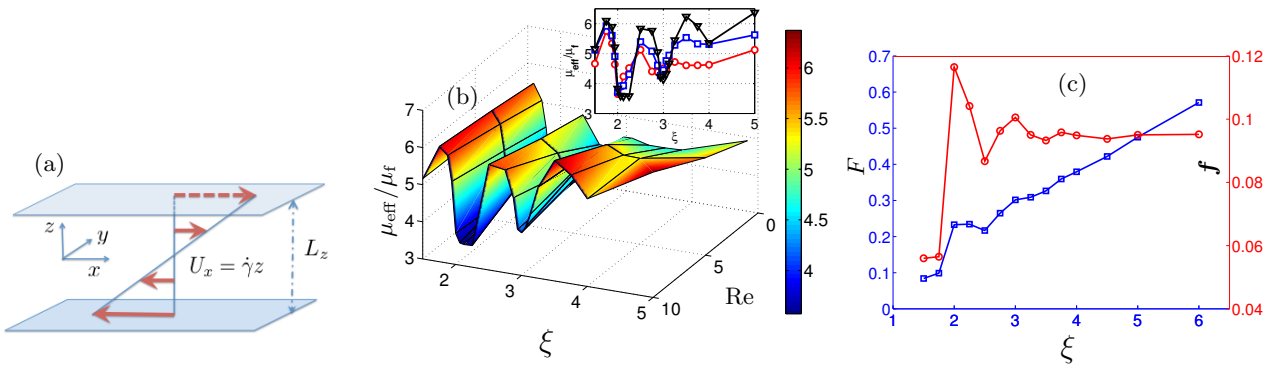


FIG. 1. (a) A sketch of the domain. (b) Surface plot of the effective viscosity $\mu_{\rm eff}/\mu_{\rm f}$ as a function of ξ and Re for $\phi = 0.3$. The inset shows $\mu_{\rm eff}/\mu_{\rm f}$ versus ξ for $\phi = 0.3$ and for three different values of Re $= 1$ (red circles), 5 (blue squares) and 10(black triangles). (c) The flow rate of matter (both solvent and additive) F (blue squares, left vertical axis), defined in (1), and the flow-rate-per-unit-cross-section, f, (red circles, right vertical axis) as a function of ξ, for Re $= 5$ and $\phi = 0.3$.

that are equal to the local fluid velocity, which is taken to be the laminar Couette profile, Fig. (1a). We calculate the effective viscosity, $\mu_{\rm eff}$, as the ratio between the tangential stress at the walls and the shear $\dot{\gamma}$ averaged over the walls and over time. See supplemental material for further details of measurement and estimate of errors.

The effective viscosity $\mu_{\rm eff}$ is shown in Fig. (1)b as a function of Re and ξ, for $\phi = 0.3$. For large channel widths, e.g., $\xi = 5$, and large volume-fractions, e.g, $\phi \geq 0.2$, we obtain shear-thickening [see Supplemental Material Fig. (6)] as was found earlier in Ref. [7].

Here we address how confinement affects the rheology. Experiments [17], in agreement with earlier analytical calculations [18], have found that at small volume-fraction ($\phi \leq 0.15$), $\mu_{\rm eff}$ increases as ξ decreases. Our results [Supplemental Material, Fig. (6)] also supports this conclusion. Furthermore, our simulations can access hitherto unstudied higher values of volume-fraction ($\phi \geq 0.2$) for which this trend seems to reverse, i.e., $\mu_{\rm eff}$ decrease with confinement, see e.g., Supplemental Material, Fig. (6). On deeper scrutiny, a more striking picture emerges. As we show in Fig. (1b), for $\phi = 0.3$, at or near small *integer* values of ξ ($\xi = 2, 3$, and 4), the effective viscosity drops significantly. In our simulations, the minimum value of viscosity is found at $\xi = 2$, which is as low as 50% of its bulk value ($\xi \geq 6$).

To appreciate how dramatic this effect is, we measure the (dimensionless) flux of matter (i.e. both the fluid and the spheres) through the channel, defined as [19] -

$$F \equiv \frac{1}{\dot{\gamma} L_z a^2} \rho \langle \int \boldsymbol{U}_x p(z) dy dz \rangle; \qquad (1)$$

where $\boldsymbol{U} \equiv \zeta \boldsymbol{U}^{\rm p} + (1-\zeta)\boldsymbol{u}$, with $\zeta = 1$ at a grid point inside a rigid sphere but $\zeta = 0$ otherwise [20], Here, $\boldsymbol{U}^{\rm p}$ is the velocity of the sphere, $\boldsymbol{u}$ is the velocity of the fluid, $p(z) = 1$ for $z \geq 0$ and -1 for $z < 0$, and $\langle \cdot \rangle$ denotes averaging over time. In Fig. (1c) we report F as a function of ξ. As the flux F is not normalized by the cross-sectional area of the channel it is expected to increase linearly as a function of ξ. This expectation indeed holds for $\xi > 4$. But, below that, for integer values of ξ the effective viscosity can decrease so much that F is not even a monotonic function of ξ, in particular, $F(\xi = 2) > F(\xi = 2.5)$; the flux through a wider channel is actually smaller. The flux-per-unit-area, $\boldsymbol{f} \equiv F(a^2/L_y L_z)$, shown in Fig. (1c) is expectedly a constant at large ξ. For the small integer values of ξ, it is significantly higher than its bulk value.

To investigate the mechanism behind the rheology, we examine snapshots of the spheres, see Fig. (2a) for $\xi = 2$ (top) and $\xi = 2.5$ (bottom). The spheres are color-coded by their initial wall-normal locations (red corresponds to an initial position near the top boundary and blue to the bottom boundary). It can be clearly observed, that for $\xi = 2$, the particles form a bi-layered structure. This layering is also confirmed by the wall-normal profiles of the average particle number density displayed in Fig. (2b) for $\xi = 2, 2.5$ and 3. In the first and the last case, one can observe equally-spaced two and three prominent peaks respectively. Note that a weaker layering is observed for $\xi = 2.5$. The drop in effective viscosity thus corresponds to the formation of layers that slide on each other, with little transport of momentum across the layers. For $\xi = 2$, where layering is most prominent, the particles form disordered liquid-like structures, within each layer, as seen by the radial distribution function of the position of the spheres, see Supplemental Material, Fig. (7).

In order to understand the dynamics of particles in the wall-normal direction, we show in Fig. (3a), the probability distribution function (PDF) of the displacement of the spheres, $d_{\rm z}(t) \equiv z_{\rm c}(t) - z_{\rm c}(0)$, at different times, where $z_{\rm c}(t)$ is the the z coordinate of the center of a sphere. Obviously, as $t \to 0$ the PDF $[P(d_{\rm z})]$ must approach a Dirac delta function. Remarkably, for $\xi = 2$ the PDF has exponential tails, i.e., it is non-diffusive, with some particles undergoing larger displacements as shown in Fig. (3a). At later times, for $\xi = 2$, the PDF of $d_{\rm z}$ develops a

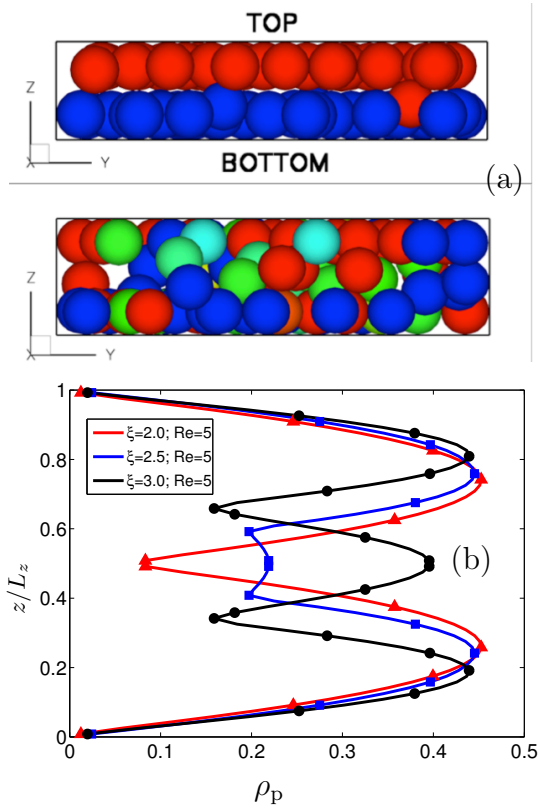


FIG. 2. (a) Three dimensional view of positions of the spheres for Re = 5, $\phi = 0.3$ and $\xi = 2$ (top) and $\xi = 2.5$ (bottom) at later times after the initial transients. The particles are color coded by their initial wall-normal position. (red: close to the top boundary, blue: close to the bottom boundary). (b) Average local density of spheres ρ_p versus the wall-normal coordinate z, for $\xi = 2$ (red triangles), 2.5 (blue squares), and 3 (black dots).

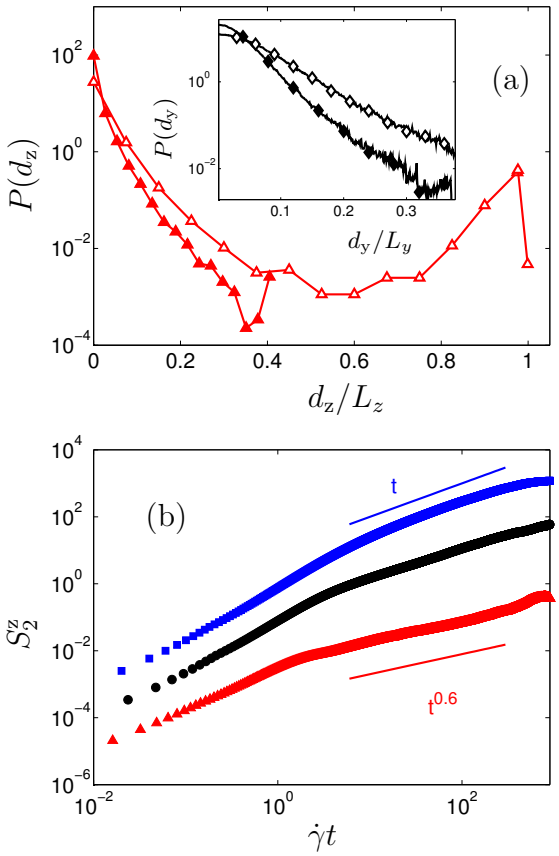


FIG. 3. (a) The PDF, $P(d_z)$, of the displacement (d_z) of the center of the spheres along the z direction for $\xi = 2$, at early times, $t = 2.5\dot{\gamma}^{-1}$ (red, filled triangles) and late times $t = 386\dot{\gamma}^{-1}$ (red, open triangles). For comparison, the inset shows the PDF, $P(d_y)$, of the displacement (d_y) along the y direction at early times, $t = 2.5\dot{\gamma}^{-1}$ (black, filled diamonds) and late times $t = 5\dot{\gamma}^{-1}$ (black, open diamonds) (b) Log-log plot of mean square displacement of the spheres, S_2^z, versus $t\dot{\gamma}$. At late times, $S_2^z \sim t^\beta$, where $\beta = 1$ implies diffusion. For three different values of $\xi = 2$ (red triangles), 2.5 (blue squares) and 3 (black dots), we obtain $\beta \approx 0.61$, 0.95 and 0.88, respectively.

peak at $d_z/L_z = 1$, indicating the hopping between two layers. A similar behavior is observed for $\xi = 3$ too. Contrast this result with the PDF of the displacement along the span-wise(y) direction, inset of Fig. (3a), which clearly shows Gaussian behavior at all times, implying diffusive dynamics. The second moment of these PDFs provides the mean squared displacement of the particles, $S_2^z(t) = \langle[z_c(t) - z_c(0)]^2\rangle_p$, the time evolution of which is shown in Fig. (3b). At late times, in general, a power-law dependence on time is found, $S_2^z(t) \sim t^\beta$, where $\beta = 1$ would imply a simple diffusive behavior. For $\xi = 2, 3$ we estimate $\beta \approx 0.61$ and 0.88 respectively. But for $\xi = 2.5$, $\beta \approx 1$ is obtained. The diffusive behaviour for $\xi = 2.5$ can be further confirmed by plotting the PDF of d_z. At intermediate times ($t = 2.5\dot{\gamma}^{-1}$), for $\xi = 2.5$, the PDF develops Gaussian tails, indicative of a diffusive process and at late times it approaches a constant (see Supplemental Material, Fig. (8)).

To visualize the dynamics, we provide movies of the particles' trajectories (available at `https://www.youtube.com/watch?v=Qn4DiXZFsbw` for the case $\xi = 2$ and at `https://www.youtube.com/watch?v=AmNsAsY0eC8` for the case $\xi = 2.5$). These clearly demonstrate that for $\xi = 2$, each horizontal layer is structurally disordered but dynamically frozen. We quantify this phenomenon by three different measurements:

(A) We calculate the residence time (τ) of a sphere in a single layer. A sphere is considered to reside within a horizontal layer till the wall-normal coordinate of its center, z_c, is within a distance of $2a$ of its initial position. Instead of calculating the PDF by histograms of τ, we calculate the cumulative PDF, $Q(\tau)$, by the rank-order method [21], as the latter is free from binning errors. The cumulative PDF, $Q(\tau)$, is displayed in Fig. (4a) as a function of τ for $\xi = 2$ and 2.5 for Re = 1 and 5. For

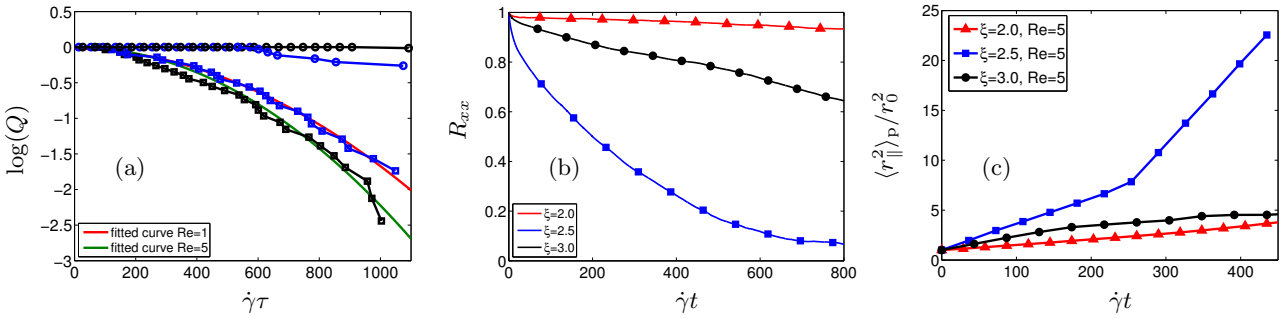


FIG. 4. (a) Cumulative PDF, Q, of the residence times of spheres ($\dot{\gamma}\tau$) in a layer for $\phi = 0.3$, Re $= 1$ (in blue) , and Re $= 5$ (in black) and $\xi = 2$ (circles), and $\xi = 2.5$ (squares). (b) The streamwise velocity-velocity auto-correlation function, R_{xx}, for Re $= 5$ and $\phi = 0.3$ for four different values of $\xi = 2$(red triangles), 2.5 (blue squares), and 3 (black dots). (b) Evolution of averaged square of relative distance between pairs of sphere, $\langle r_\parallel^2(t, r_0)\rangle_{\rm p}$ which were at distance r_0 at $t = 0$; for $r_0 = 4a$, for three different values of $\xi = 2$ (red triangles), 2.5 (blue squares), and 3 (black dots).

$\xi = 2$, Q remains very close to unity during the whole duration of the simulation, i.e., very few spheres actually move from one layer to another. In other words, the layers are quite stable to perturbations in wall-normal directions. Conversely for $\xi = 2.5$, $Q(\tau)$ can be fitted by a Gaussian.

(B) The streamwise velocity auto-correlation function of the spheres, $R_{xx} \equiv \langle U_x^{\rm p}(t)U_x^{\rm p}(0)\rangle$, is shown in Fig. (4)b. For $\xi = 2$, $R_{xx} \approx 1$ for a very long time, implying that the temporal fluctuations of the stream-wise velocity are negligible. This suggests that each sphere moves in a layer with a uniform stream-wise velocity keeping their relative distances practically constant. For the cases where the layering is not very strong, e.g., $\xi = 2.5$ the auto-correlation function decays rapidly. For $\xi = 3$, layering reappears and R_{xx} again shows slow decay in time.

(C) Let us define $r_\parallel(t; r_0)$ to be the (horizontal) distance between a pair of spheres at time t, which were at a (horizontal) distance r_0 and $t = 0$. If the layers formed by the spheres were truly frozen-in-time we would obtain $r_\parallel(t; r_0) = r_0$ for all t and r_0. In Fig. (4c), we show the time evolution of $\langle r_\parallel^2(t; r_0)\rangle_{\rm p}$, for $r_0 = 4a$, where the symbol $\langle\cdot\rangle_{\rm p}$ denotes averaging over all possible particle pairs [22]. Had the spheres moved chaotically within a layer, $r_\parallel$ would have grown exponentially with time. Clearly for all the cases shown in Fig. (4c), $r_\parallel$ grows at most linearly with time. In particular, when layering occurs ($\xi = 2, 3$), it takes a long time ($t \geq 430\dot{\gamma}^{-1}$) for $r_\parallel(t; 4a)$ to grow by a factor of two. This quantifies again the dynamical stability of the layer, the relative in-plane distance between pairs of spheres change slowly (linearly) with time.

In conclusion, using numerical simulations, we demonstrate that the effective viscosity of an extremely confined non-Brownian suspension can exhibit a non-monotonic dependence on the channel width, in particular the effective viscosity sharply decreases if the channel width is an (small) integer multiple of particle diameter. We demonstrate that this behavior is accompanied by a change in micro-structure, namely the formation of particle layers parallel to the confining plates. The two-dimensional layers formed by the particles slide on each other, the layers are structurally liquid-like by evolve on very show time scales. Similar layering under shear, have been theoretically anticipated [23], but the consequences for transport in extreme confinement as shown by us has never been demonstrated before. We finally note that our results are in contrast with the case of sheared Brownian suspensions where the structure was found to be uncorrelated with measured viscosity [24].

ACKNOWLEDGMENT

LB and WF acknowledge financial support by the European Research Council Grant No. ERC-2013-CoG-616186, TRITOS and computer time provided by SNIC (Swedish National Infrastructure for Computing). DM acknowledges financial support from Swedish Research Council under grant 2011-542 (DM) . PC thanks NORDITA for hospitality.

[1] N. J. Wagner and J. F. Brady, Physics Today **64**, 27 (2009).
[2] J. J. Stickel and R. L. Powell, Annu. Rev. Flu. Mech. **37**, 129 (2005).
[3] G. Batchelor, An Introduction to Fluid Dynamics (Cambridge University Press, Cambridge, UK, 1967).
[4] A. Einstein, Annln. Phys. **19**, 298 (1906).
[5] J. F. Brady, International Journal of Multiphase Flow **10**, 113 (1983).
[6] A. Fall, A. Lemaître, F. Bertrand, D. Bonn, and G. Ovarlez, Phys. Rev. Lett. **105**, 268303 (2010).
[7] F. Picano, W.-P. Breugem, D. Mitra, and L. Brandt, Phys. Rev. Lett. **111**, 098302 (2013), arXiv:1211.5501

[physics.flu-dyn].
[8] E. Brown and H. M. Jaeger, Phys. Rev. Lett. **103**, 086001 (2009).
[9] N. Fernandez, Phys. Rev. Lett. **111**, 108301 (2013).
[10] E. *et al.* Brown, Journal of Rheology **54**, 1023 (2010).
[11] D. Di Carlo, Lab on a Chip **9**, 3038 (2009).
[12] W. Lee, H. Amini, H. A. Stone, and D. Di Carlo, Proceedings of the National Academy of Sciences **107**, 22413 (2010).
[13] D. Di Carlo, J. F. Edd, K. J. Humphry, H. A. Stone, and M. Toner, Physical review letters **102**, 094503 (2009).
[14] H. Amini, E. Sollier, W. M. Weaver, and D. Di Carlo, Proceedings of the National Academy of Sciences **109**, 11593 (2012).
[15] C. Peskin, Acta Numerica **11**, 479 (2002).
[16] R. Mittal and G. Iaccarino, Annu. Rev. Fluid Mech. **37**, 239 (2005).
[17] P. Peyla and C. Verdier, Europhys. Lett. **94**, 44001 (2011).
[18] Y. Davit and P. Peyla, Europhys. Lett. **83**, 64001 (2008).
[19] F. Picano, W.-P. Breugem, and L. Brandt, J. Flu. Mech. **764**, 463 (2015).
[20] The phase indicator ζ is is related to the volume fraction by $\phi = (1/V)\int \zeta dV$ where V is the total volume of the channel.
[21] D. Mitra, J. Bec, R. Pandit, and U. Frisch, Phys. Rev. Lett **94**, 194501 (2005).
[22] To take into account the movement of the spheres across layers, we calculate $r_\parallel$ up to the time it takes for the wall-normal distance between the pair of spheres to become larger than $2a$.
[23] M. Zurita-Gotor, J. Bawzdziewicz, and E. Wajnryb, Phys. Rev. Lett. **108**, 068301 (2012).
[24] X. Xu, S. Rice, and A. Aaron R. Dinner, PNAS **110**, 3771 (2012).
[25] W.-P. Breugem, Journal of Computational Physics **231**, 4469 (2012).

Supplemental Material

Here we provide supplemental material for our paper. The material is divided into several subsections.

Direct numerical simulation

Simulations have been performed using the numerical code originally described in Ref. [25] that fully describes the coupling between the solid and fluid phases. The Eulerian fluid phase is evolved according to the incompressible Navier-Stokes equations,

$$\boldsymbol{\nabla}\cdot\boldsymbol{u} = 0 \tag{A.2}$$

$$\partial_t \boldsymbol{u} + \boldsymbol{u}\cdot\boldsymbol{\nabla}\boldsymbol{u} = -\frac{1}{\rho}\boldsymbol{\nabla}p + \nu\nabla^2\boldsymbol{u} + \boldsymbol{f} \tag{A.3}$$

where $\boldsymbol{u}$, ρ and $\nu = \mu/\rho$ are the fluid velocity, density and kinematic viscosity respectively (μ is the dynamic viscosity), while p and $\boldsymbol{f}$ are the pressure and a generic force field (used to model the presence of particles). The particles centroid linear and angular velocities, $\boldsymbol{U}^{\mathrm{p}}$ and $\boldsymbol{\Omega}^{\mathrm{p}}$ are instead governed by the Newton-Euler Lagrangian equations,

$$\rho_{\mathrm{p}} V_{\mathrm{p}} \frac{d\boldsymbol{U}^{\mathrm{p}}}{dt} = \rho \oint_{\partial\mathcal{V}_{\mathrm{p}}} \boldsymbol{\tau}\cdot\boldsymbol{n}\, dS \tag{A.4}$$

$$\mathcal{I}_{\mathrm{p}} \frac{d\boldsymbol{\Omega}^{\mathrm{p}}}{dt} = \rho \oint_{\partial\mathcal{V}_{\mathrm{p}}} \boldsymbol{r}\times\boldsymbol{\tau}\cdot\boldsymbol{n}\, dS \tag{A.5}$$

where $V_{\mathrm{p}} = 4\pi a^3/3$ and $\mathcal{I}_{\mathrm{p}} = 2\rho_{\mathrm{p}} V_{\mathrm{p}} a^2/5$ are the particle volume and moment of inertia; $\boldsymbol{\tau} = -p\boldsymbol{I} + 2\mu\boldsymbol{E}$ is the fluid stress, with $\boldsymbol{E} = \left(\boldsymbol{\nabla}\boldsymbol{u} + \boldsymbol{\nabla}\boldsymbol{u}^{\mathrm{T}}\right)/2$ the deformation tensor; $\boldsymbol{r}$ is the distance vector from the center of the sphere while $\boldsymbol{n}$ is the unity vector normal to the particle surface $\partial\mathcal{V}_p$. Dirichlet boundary conditions for the fluid phase are enforced on the particle surfaces as $\boldsymbol{u}|_{\partial\mathcal{V}_p} = \boldsymbol{U}^{\mathrm{p}} + \boldsymbol{\Omega}^{\mathrm{p}}\times\boldsymbol{r}$.

An immersed boundary method is used to couple the fluid and solid phases. The boundary condition at the moving particle surface is modeled by adding a force field on the right-hand side of the Navier-Stokes equations. The fluid phase is therefore evolved in the whole computational domain using a second order finite difference scheme on a staggered mesh while the time integration is performed by a third order Runge-Kutta scheme combined with a pressure-correction method at each sub-step. This integration scheme is also used for the Lagrangian evolution of eqs. (A.4) and (A.5). Rach particle surface is described by uniformly distributed N_{L} Lagrangian points. The force exchanged by the fluid on the particles is imposed on each $l-th$ Lagrangian point. This force is related to the Eulerian force field $\boldsymbol{f}$ by the expression $\boldsymbol{f}(\boldsymbol{x}) = \sum_{l=1}^{N_L} F_{\mathrm{l}}\delta^3(\boldsymbol{x}-\boldsymbol{X}_{\mathrm{l}})\Delta V_l$ (where ΔV_{l} is the volume

of the cell containing the $l-th$ Lagrangian point while δ^3 is the three dimensional Dirac delta distribution). The force field is calculated through an iterative algorithm that ensures a second order global accuracy in space. In order to maintain accuracy, eqs. (A.4) and (A.5) are rearranged in terms of the IBM force field,

$$\rho_{\rm p} V_{\rm p} \frac{d\boldsymbol{U}^{\rm p}}{dt} = -\rho \sum_{l=1}^{N_l} F_{\rm l} \Delta V_{\rm l} + \rho \frac{d}{dt} \int_{\mathcal{V}_{\rm p}} \boldsymbol{u}\, dV \tag{A.6}$$

$$\mathcal{I}_{\rm p} \frac{d\boldsymbol{\Omega}^{\rm p}}{dt} = -\rho \sum_{l=1}^{N_l} \boldsymbol{r}_{\rm l} \times F_{\rm l} \Delta V_{\rm l} + \rho \frac{d}{dt} \int_{\mathcal{V}_{\rm p}} \boldsymbol{r} \times \boldsymbol{u}\, dV \tag{A.7}$$

where $\boldsymbol{r}_{\rm l}$ is the distance from the center of a particle. The second terms on the right-hand sides are corrections to account for the inertia of the fictitious fluid contained inside the particles. Lubrication models based on Brenner's asymptotic solution gare used to correctly reproduce the interaction between two particles when the gap distance between the two is smaller than twice the mesh size. A soft-sphere collision model is used to account for collisions between particles and between particles and walls. An almost elastic rebound is ensured with a restitution coefficient set at 0.97. These lubrication and collision forces are added to the right-hand side of eq. (A.6).
The code has been validated against several classic test cases [25] and has been used earlier to study shear-thickening in inertial suspensions in Ref. [7].

Measurement of effective viscosity

We calculate the effective viscosity as the ratio between the tangential stress at the walls and $\dot{\gamma}$. The tangential stress, and consequently the effective viscosity, is different at different points of the wall and also at each point changes as a function of time. At each time, we calculate the average of this effective viscosity over the walls and obtain a time-series $\mu_{\rm eff}(t)$. This time-series is displayed in Fig. (5) for one particular case. Clearly, after a short while the effective viscosity reaches a stationary value with fluctuations about it. Typically, we find that our simulations reach statistically stationary state when time $t \geq 200\dot{\gamma}^{-1}$ The average of $\mu_{\rm eff}(t)$ over this statistically stationary state is the effective viscosity $\mu_{\rm eff}$ and the standard deviation of the fluctuations is used as an estimate of the error in the measurement of $\mu_{\rm eff}$ as reported in TableI A careful look at the table will convince the reader that the relative strength of the fluctuations decreases at commensuration.

ξ	$\mu_{\rm eff}/\mu_{\rm f}$ (Re = 1)	$\mu_{\rm eff}/\mu_{\rm f}$ (Re = 5)	$\mu_{\rm eff}/\mu_{\rm f}$ (Re = 10)
1.5000	4.665 ± 0.113	5.123 ± 0.079	5.161 ± 0.107
1.7500	5.758 ± 0.116	5.925 ± 0.114	6.100 ± 0.115
1.8750	5.334 ± 0.186	5.603 ± 0.190	5.895 ± 0.173
1.9375	4.641 ± 0.190	4.906 ± 0.234	5.213 ± 0.209
2.0000	3.650 ± 0.120	3.709 ± 0.058	3.831 ± 0.066
2.0625	3.888 ± 0.152	3.916 ± 0.143	3.596 ± 0.075
2.1250	4.237 ± 0.183	3.928 ± 0.139	3.574 ± 0.100
2.2500	4.517 ± 0.141	4.308 ± 0.244	3.581 ± 0.087
2.5000	5.129 ± 0.165	5.396 ± 0.189	5.836 ± 0.181
2.7500	4.403 ± 0.162	5.083 ± 0.163	5.766 ± 0.158
2.8750	4.381 ± 0.147	4.609 ± 0.138	5.051 ± 0.148
2.9375	4.303 ± 0.147	4.261 ± 0.120	4.223 ± 0.102
3.0000	4.506 ± 0.155	4.446 ± 0.130	4.148 ± 0.180
3.0625	4.462 ± 0.177	4.763 ± 0.148	4.326 ± 0.223
3.1250	4.718 ± 0.185	4.942 ± 0.171	4.670 ± 0.237
3.2500	4.721 ± 0.184	5.286 ± 0.160	5.449 ± 0.172
3.5000	4.608 ± 0.165	5.535 ± 0.166	6.238 ± 0.189
3.7500	4.610 ± 0.168	5.326 ± 0.142	5.923 ± 0.166
4.0000	4.629 ± 0.156	5.323 ± 0.154	5.358 ± 0.176
5.0000	5.150 ± 0.208	5.626 ± 0.152	6.371 ± 0.193
6.0000	4.752 ± 0.180	5.816 ± 0.143	6.807 ± 0.173

TABLE I. Values of $\mu_{\rm eff}/\mu_{\rm f}$ obtained at different ξ and Re with respective error.

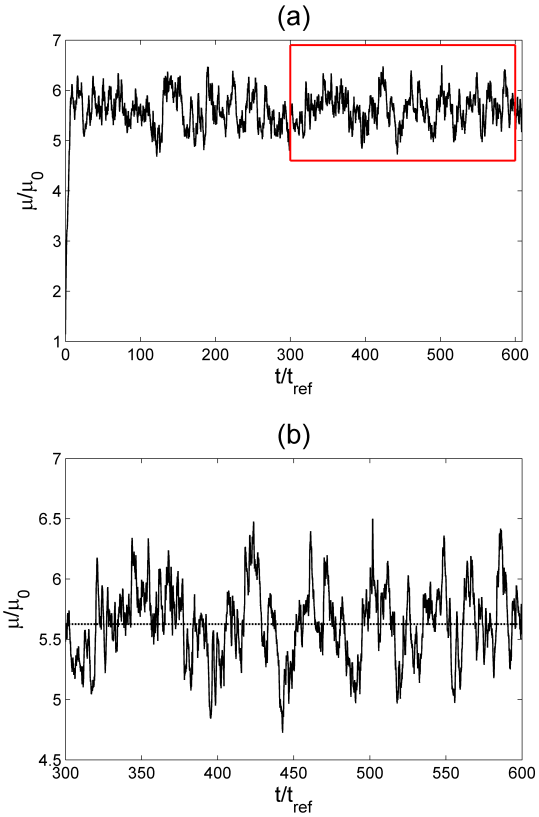


FIG. 5. The effective viscosity $\mu_{\rm eff}(t)$ (normalized by the viscosity of the solvent) as a function of time for one representative run.

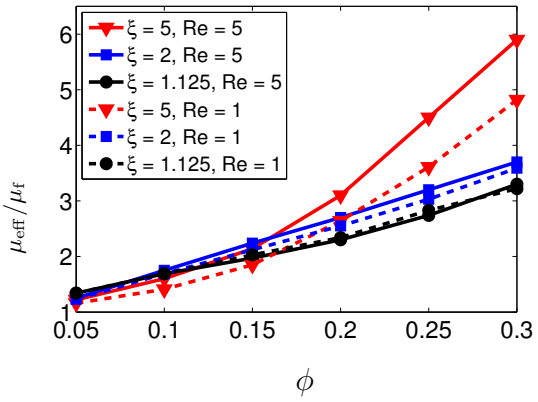


FIG. 6. The effective viscosity $\mu_{\rm eff}/\mu_{\rm f}$ versus ϕ for two different values of Re = 1 (dashed lines) and 5 (continuous lines) for three different values of $\xi = 1$ (black filled circles), 2 (blue squares) and 5 (red triangles).

Effective viscosity as a function of volume fraction

Here we show, see Fig. (6), the variation of the effective viscosity, $\mu_{\rm eff}$ as a function of the volume fraction, ϕ.

In-layer radial distribution function

The radial distribution function of the position of the centers of the spheres in the $x-y$ plane is shown in Fig. (7). This is defined as

$$R_{\parallel} \equiv \frac{1}{2\pi r \Delta z n_0} \frac{dN_r}{dr} \tag{A.8}$$

where N_r is the number of particles is the number of particles in a cylinder of radius r and $n_0 = N_p(N_p - 1)/(2V)$ is the density of particles pairs in a volume V with N_p the total number of particles.

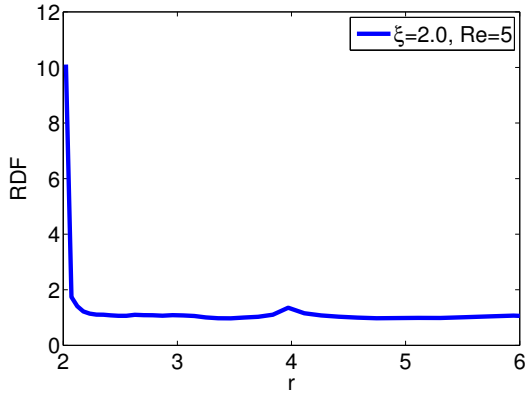


FIG. 7. The radial distribution function of the position of the centers of the spheres in the $x-y$ plane.

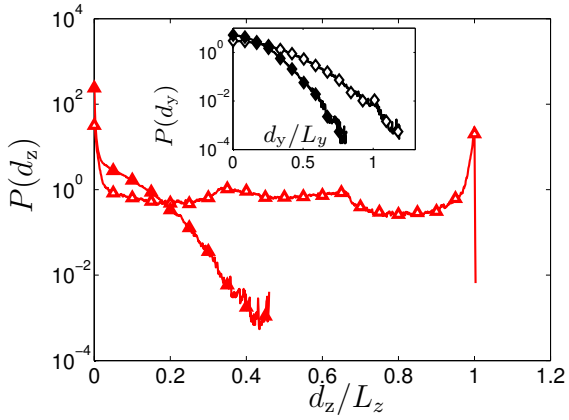


FIG. 8. The PDF ($P(d_z)$) of the displacement (d_z) of the center of the spheres along the z direction, for $\xi = 2.5$, at early times, $t = 2.5\dot{\gamma}^{-1}$ (red, filled triangles) and late times $t = 386\dot{\gamma}^{-1}$ (red, open triangles). For comparison, the inset shows the PDF ($P(d_y)$) of the displacement (d_y) along the y direction at early times, $t = 2.5\dot{\gamma}^{-1}$ (black, filled diamonds) and late times $t = 5\dot{\gamma}^{-1}$ (black, open diamonds)